Localization of Wannier functions for entangled energy bands

U. Birkenheuer* and D. Izotov†
Max-Planck-Institut für Physik komplexer Systeme, Nöthnitzer Strasse 38, 01187 Dresden, Germany
(Received 5 October 2004; revised manuscript received 7 December 2004; published 21 March 2005)

A method for the localization of crystalline orbitals for entangled energy bands is proposed. It is an extension of the Wannier-Boys algorithm [C. M. Zicovich-Wilson, R. Dovesi, and V. R. Saunders, J. Chem. Phys., **115**, 9708 (2001)] which is particularly well suited for linear combination of atomic orbital representations of the Bloch waves. It allows the inclusion of additional bands during the optimization of the unitary hybridization matrix used in the multiband Wannier transformation. By a projection technique, the proper chemical character is extracted from the Bloch waves and compact localized orbitals are obtained even for entangled bands. The performance of our projective Wannier–Boys localization is demonstrated on the low-lying unoccupied bands of trans-polyacetylene, diamond, and silicon. The π bands of graphene are discussed as well.

DOI: 10.1103/PhysRevB.71.125116 PACS number(s): 71.15.Ap, 71.15.Dx

I. INTRODUCTION

Localization of Wannier functions (WFs) has attracted great attention of scientists in recent years. Despite the success of describing most of the physical phenomena in crystals in terms of Bloch waves (BWs), WFs (Ref. 1) have obvious advantages. To mention a few: WFs provide a chemically intuitive picture of the electronic structure in crystals, using localized WFs, physical quantities such as effective Born charges and spontaneous polarization can be evaluated in a very simple way,[2–4] and they play a central role in many post-Hartree-Fock electron correlation methods.[5–9] In fact, orbital localization schemes, both for solids and molecules, have a long tradition as can be seen, for example, from Refs. 10 and 11; two of the early key references.

Several rigorous procedures for the localization of WFs have been proposed so far. They fall into two categories, those which are based on the variational principle,[12,13] and those which are an extension of the Foster-Boys localization criterion[14,15] for periodic systems.[16–19] For the latter class, it is important to find a rigorous way of defining the expectation value $\langle \boldsymbol{r} \rangle$ of the position operator for periodic systems which is by no means trivial.[20] All of these localization methods can only be applied to isolated band complexes, i.e., a group of bands which are separated from the other bands by an energy gap over the *entire* Brillouin zone. This restriction appreciably confines the possible applications of those methods and only a limited number of systems can be treated. In particular, the energy bands of the unoccupied Bloch waves usually do not exhibit any such band gaps. Thus, none of the localization schemes developed so far can be applied routinely to selectively generate virtual WFs as needed, for instances, in our wave-function-based post-Hartree-Fock correlation methods for valence *and* conduction bands.[21,22]

Recently, Souza *et al.*[23] have extended the original Marzari-Vanderbilt localization scheme[16] to systems with entangled bands. The method is based on a preselection of optimal Bloch waves having maximal similarity at neighboring k points by minimizing a suitable functional. Like the original scheme, the new method is especially designed for a plane wave representation of the BWs and heavily relies on numerical k-space differentiations.

In this paper, we propose a similar extension for the Wannier-Boys (WB) localization scheme developed by Zicovich-Wilson *et al.*[19] This scheme differs in many aspects from the algorithm proposed by Marzari *et al.*[16] In particular, it is much better suited for BWs given in a linear combination of atomic orbital (LCAO) representation as employed in many widely used program packages for periodic systems such as CRYSTAL,[24] GAUSSIAN,[25] DMOL[3] (Ref. 26), NFP-LMTO,[27] or ADF-BAND.[28,29]

In Sec. II, the details of our algorithm are described. Then, in Sec. III, the results from the localization are presented for *trans*-polyacetylene (*t*-PA), diamond, and silicon, and some concluding remarks are drawn in Sec. IV.

II. THE LOCALIZATION PROCEDURE

The projective WB scheme we want to present here sets out from the original WB localization procedure which is discussed in detail in Ref. 19. Like all localization schemes for composite bands, it relies on the initial specification of a fixed set of energy bands. These bands determine the space of the Bloch functions which are allowed to participate in the multiband Wannier transformation, the so-called active space. For example, the valence bands of a system can be chosen as such a set of bands. The WB algorithm is a combination of two steps: The so-called "Wannierization" and a Foster-Boys localization of the obtained WFs within the reference unit cell. Recently, the algorithm has been extended to operate with a multicell Foster-Boys localization to better preserve the space group symmetry of the system under consideration.[30]

The Wannierization step starts from a set of trial WFs $\omega_s^{(0)}(\boldsymbol{r})$ in LCAO representation

$$\omega_s^{(0)}(\boldsymbol{r}) = \sum_{\mu,\boldsymbol{R}} c_{\mu s}^{\boldsymbol{R}} \phi_\mu(\boldsymbol{r} - \boldsymbol{s}_\mu - \boldsymbol{R}). \tag{1}$$

We follow the notation from Ref. 19 here. Thus, μ runs over all atomic basis functions $\phi_\mu(\boldsymbol{r}-\boldsymbol{s}_\mu)$ in the reference unit cell,

$\boldsymbol{s}_\mu$ denotes their centers, and $\boldsymbol{R}$ runs over all lattice vectors of the underlying Bravais lattice. To reduce the spatial extent of each of these WFs, the orbital coefficients $c_{\mu s}^{\boldsymbol{R}}$ are set to zero for all sites $\boldsymbol{s}_\mu+\boldsymbol{R}$ at which the atomic Mulliken populations[31,32] of the given WF falls below a certain threshold (for details, see Ref. 19). The WFs obtained this way, the so-called "model functions,"[19] are transformed to k space, projected onto the active space spanned by the selected BWs, orthonormalized again, transformed back to real space, and moved back into the reference unit cell (if necessary). The resulting (real) WFs, $\bar{\omega}_s^{(1)}$, then enter the Foster-Boys step, where they are subject to an orthogonal transformation

$$\omega_s^{(1)} = \sum_{t=1}^{N} \bar{\omega}_t^{(1)} O_{ts} \tag{2}$$

that minimizes the spread $\Omega[\{\omega_s^{(1)}\}]$ given by the functional

$$\Omega[\{\omega_s\}] = \sum_{s=1}^{N} (\langle\omega_s|r^2|\omega_s\rangle - \langle\omega_s|\boldsymbol{r}|\omega_s\rangle^2). \tag{3}$$

Here, N is the number of energy bands involved in the localization. Finally, the optimized functions $\omega_s^{(1)}$ are used as new (orthonormal) trial functions for the Wannierization and the whole procedure is repeated until convergence is reached. The discarding of orbital coefficients and the subsequent projection onto the active space is the crucial part of the WB algorithm. It is combined with a Foster-Boys localization to ensure localization of the WFs also *inside* the unit cells.

The described algorithm performs well for isolated band complexes. In the case of entangled bands, however, the selection of proper bands to set up a suitable active space becomes problematic. Avoided and symmetry-allowed crossings between the energy bands in mind and other disturbing energy bands occur, and the orbital character we are looking for is spread over several BWs which in turn exhibits more or less strong admixtures from other contaminating orbitals. To overcome these difficulties, we give up the concept of a rigid active space, abandon the constraint that the number of selected BWs per k point has to coincide with the number N of Wannier functions per unit cell, and allow additional BWs to be included in the active space at each k point.

The selection of an appropriate N-dimensional active subspace is then done in the projection step during the Wannierization. To this end, the "model BWs"

$$\xi_{s\boldsymbol{k}}(\boldsymbol{r}) = \sum_{\boldsymbol{R}} e^{i\boldsymbol{k}\boldsymbol{R}} \xi_s(\boldsymbol{r}-\boldsymbol{R}), \tag{4}$$

which are the k-space transforms of the model functions $\xi_s(\boldsymbol{r})$, are projected onto the active space via

$$\xi'_{s\boldsymbol{k}} = \sum_{n=1}^{N_{\boldsymbol{k}}} \psi_{n\boldsymbol{k}} \langle\psi_{n\boldsymbol{k}}|\xi_{s\boldsymbol{k}}\rangle \text{ for } s = 1, \ldots N \tag{5}$$

with the number $N_{\boldsymbol{k}}$ of selected BWs $\psi_{n\boldsymbol{k}}$ at each k point being at least as large as the number of WFs per unit cell. The matrices $U_{ns}(\boldsymbol{k}) = \langle\psi_{n\boldsymbol{k}}|\xi_{s\boldsymbol{k}}\rangle$ showing up here establish a generalization of the unitary hybridization matrices used in conventional multiband Wannier transformations.[10] The new projected functions $\xi'_{s\boldsymbol{k}}$ are those functions in the active space which resemble the initial model BWs $\xi_{s\boldsymbol{k}}$ the most. They span the N-dimensional subspace used in the subsequent Wannier transformation. In this sense, the procedure outlined here is very similar to the one proposed by Souza *et al.*[23] In particular, our extended projection step during the Wannierization can be regarded as an analog to the band preselection scheme used in their method.

For convenience, the projected k-space transformed model functions $\xi'_{s\boldsymbol{k}}$ are subject to a symmetric or Löwdin orthonormalization,[33] resulting in a set of orthonormal BWs $\xi''_{s\boldsymbol{k}}$ which—after a band-by-band Wannier transformation—yield the WFs ω_s we are looking for. That means, the ultimate orthonormal Bloch waves $\xi''_{s\boldsymbol{k}}$ can be understood as the k space transforms of the generated Wannier functions ω_s:

$$\xi''_{s\boldsymbol{k}}(\boldsymbol{r}) = \sum_{\boldsymbol{R}} e^{i\boldsymbol{k}\boldsymbol{R}} \omega_s(\boldsymbol{r}-\boldsymbol{R}). \tag{6}$$

As for any kind of hybrid orbitals, the orbital energies

$$\varepsilon''_{s\boldsymbol{k}} = \langle\xi''_{s\boldsymbol{k}}|F|\xi''_{s\boldsymbol{k}}\rangle \tag{7}$$

of the orthonormalized projected model BWs have little in common with the canonical band energies $\varepsilon_{n\boldsymbol{k}}$ they originate from. Even the well-known sum rule

$$\sum_{s=1}^{N} \varepsilon''_{s\boldsymbol{k}} = \sum_{n=1}^{N_{\boldsymbol{k}}} \varepsilon_{n\boldsymbol{k}} \tag{8}$$

does not hold anymore, if the number $N_{\boldsymbol{k}}$ of selected BWs is larger than the number N of WFs. Yet, by diagonalizing the subblock

$$F_{st}(\boldsymbol{k}) = \langle\xi''_{s\boldsymbol{k}}|F|\xi''_{t\boldsymbol{k}}\rangle \tag{9}$$

of the Fock operator F of the system, or—which is equivalent—the Wannier representation

$$F_{st}(\boldsymbol{R}) = \langle\omega_s(\boldsymbol{r})|F|\omega_t(\boldsymbol{r}-\boldsymbol{R})\rangle, \tag{10}$$

N new, so-called disentangled energy bands $\eta_{s\boldsymbol{k}}$ are obtained. Where the contamination of the canonical BWs with orbitals of wrong character is small, the disentangled bands will essentially coincide with the canonical ones. Close to band crossings, where the contamination is larger, they will deviate substantially from the canonical bands in order to be able to follow the chemical nature of the underlying BWs. By this focus on the chemical character of the disentangled bands, an *effectively* isolated complex of N bands is formed with none of the bands showing any kinks and cones (see Sec. III for more details). The associated eigenvectors of $F_{st}(\boldsymbol{k})$ can be regarded as a sort of optimal BW hybrids with minimal orbital contamination and vanishing off-diagonal terms in the Fock operator. We will refer to these hybrids as disentangled BWs.

The WFs ω_s provide a local representation of precisely these disentangled BWs, and the corresponding representation $F_{st}(\boldsymbol{R})$ of the Fock operator of the system can be understood as an effective tight-binding or Hückel[34] description of the electronic structure of the system with special emphasize on a particular type of orbital (characterized by the active space and the initial set of model functions).

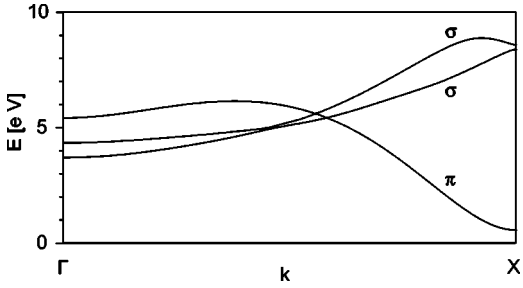

FIG. 1. Virtual Hartree-Fock bands of *t*-PA in the energy range from 0 to 10 eV calculated with a cc-pVTZ basis set (see Ref. 37).

The *canonical* BWs $\psi_{n\mathbf{k}}$, to be included in the active space, can be selected in various ways, for example, by specifying an energy window and taking all BWs whose band energies $\varepsilon_{n\mathbf{k}}$ fall into this window. Alternatively, a so-called "energy tube" around a given pair of reference bands $(\underline{n},\overline{n})$ may be used, i.e., all BWs with band energies

$$\varepsilon_{n\mathbf{k}} \in [\varepsilon_{\underline{n}\mathbf{k}} - \varepsilon, \varepsilon_{\overline{n}\mathbf{k}} + \overline{\varepsilon}] \tag{11}$$

are considered where ε and $\overline{\varepsilon}$ are some user-specified energy tolerances.

We have implemented the above projection and rediagonalization scheme as an extension to the original WB localization routine in the CRYSTAL 200x code,[35] a precursor of the most recent public version of the CRYSTAL program package.[24] Its ability to disentangle energy bands properly will be demonstrated in Sec. III where our method is applied to the virtual bands of *t*-PA, diamond and silicon.

III. RESULTS AND DISCUSSION

All band structures shown here are calculated on the Hartree-Fock level of theory. The periodic *ab initio* program package CRYSTAL (version 200x)[35] is used for that purpose. The localization of the WFs is performed a posteriori with the WB algorithm[19] as implemented in CRYSTAL 200x (Ref. 35) in conjunction with our extension for entangled bands which has been built into this version of CRYSTAL.

In all cases, we focus on the first few low-lying virtual bands of the systems. Because of the larger extent of the localized virtual Wannier functions compared to the occupied ones, the former WFs are quite sensitive to the number of k points in the Monkhorst-Pack grid.[36] We chose sufficiently fine grids to remove any ambiguities resulting from the discrete k-space integration.

A. *trans*-polyacetylene

trans-polyacetylene, —[HC═CH]$_\infty$—, suits perfectly as an illustrative example for band disentanglement, because, in the basis set employed here, it exhibits three low-lying entangled virtual bands which are separated from the rest of the unoccupied band structure (Fig. 1).

The computational parameters for *t*-PA are taken from a recent study on the correlated valence and conduction bands of *t*-PA.[21] That is, Dunning's correlation-consistent polarized valence triple-ζ basis sets (cc-pVTZ) (Ref. 37) for hydrogen and carbon (without f functions) are used, the bond distances are d(C—C)=1.45 Å, d(C═C)=1.36 Å, and d(C—H)=1.09 Å, and the bond angles are $\angle$(C—C═C)=121.7° and $\angle$(C—C—H)=118.2°. Two different geometries are considered, flat *t*-PA (the experimental structure) and a distorted configuration with the hydrogens being bent out of plane by 20° in such a way that the inversion symmetry of the polymer is preserved. The Brillouin zone is sampled by a uniform grid of 100 k points.

The first three virtual bands are selected for the disentanglement (Fig. 1). One is a π^* band formed by C═C π antibonds, the other two are of σ symmetry and describe C−H antibonds (not C−C σ antibonds, as one might think at first glance). For the flat polymer, the symmetry separation is perfect, for the distorted structure some mixture between the σ and π bonds occurs. Nevertheless, the two types of BWs remain quite different in their orbital character which should facilitate the band disentanglement significantly. In this sense, our first system very much resembles the one chosen by Souza *et al.*[23] They used copper which exhibits a d band manifold which is entangled with a single sp valence band.

Of course, for *t*-PA, one could localize the virtual BWs by means of the original WB algorithm. But what we want to demonstrate here is that it is also possible to localize the π and σ bands *separately*. We first consider the flat *t*-PA chain. In that case, the BWs come in two different symmetries and the disentanglement could simply be achieved by a proper labeling of the energy bands and the associated BWs. Yet, such symmetry classifications are hard to implement in localization schemes for periodic systems, and thus usually not exploited. Our band disentanglement algorithm, however, is able to recognize the different symmetries and to separate the bands properly.

As an initial guess for the π-type WFs, antiphase linear combinations of $2p_z$ atomic orbitals at neighboring carbon atoms are used. For the σ-type WFs, antibonding linear combinations of $2sp^2$ hybrid orbitals on carbon and $1s$ atomic orbitals on hydrogen are constructed. Because of this choice, the hybridization matrices $U_{ns}(\mathbf{k})$ become 3×1 and 3×2 matrices, respectively, with a maximum-rank subblock and all other entries being exactly zero, as is confirmed numerically.

As seen in the upper panel of Fig. 2, where the canonical band energies $\varepsilon_{n\mathbf{k}}$ are compared to the disentangled band energies $\eta_{s\mathbf{k}}$, our band disentanglement procedure is perfectly able to describe either the π or the σ orbitals alone. The crossing of the σ bands on the left-hand side is an avoided one (because of the lack of any extra symmetry in the small point group of the k points inside the Brillouin zone). The apparently extremely weak coupling of the two bands is due to "soft symmetry selection rules."[38] That means, the impact of the C−C bond length alternation in *t*-PA on the C−H antibond dominated σ^* bands is so small that they essentially behave as if there would exist an additional glide plane symmetry in the system (such as in equidistant *t*-PA). This concept is corroborated by a detailed analysis of the involved BWs.

A more interesting situation for band disentanglement arises when the symmetry of the system is lowered by moving the hydrogen atoms out of plane. Now, the three energy

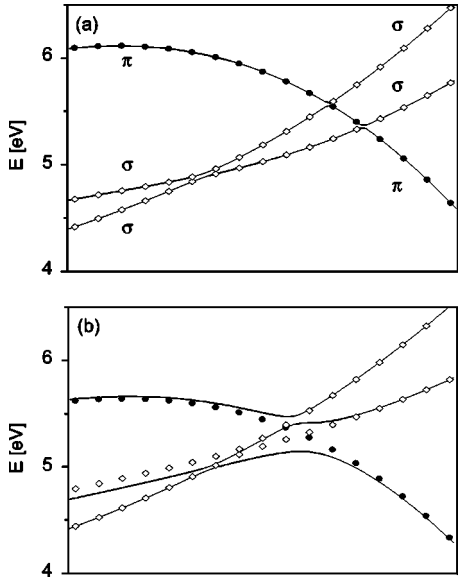

FIG. 2. Zoom into the first three virtual bands of *t*-PA along the Δ line (the endpoints of the plot correspond to one-third and two-thirds of the Γ*X* distance) for the flat (a) and the distorted (b) geometry of the polymer. Solid lines show the canonical bands, symbols represent the disentangled bands: One of π^* character (●), two of σ^* character (◇).

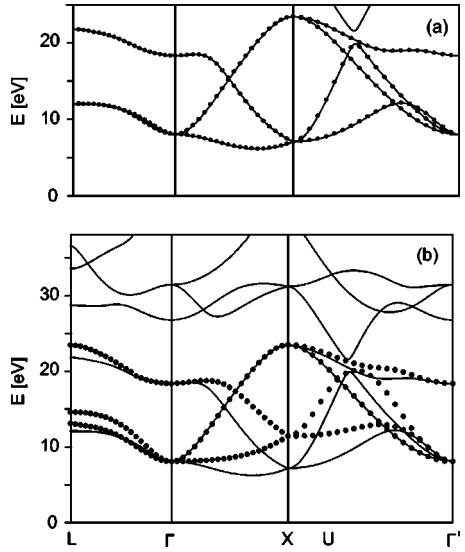

FIG. 3. Virtual band structure of diamond from a canonical Hartree-Fock calculation (solid lines) in comparison to the band energies resulting from localized Wannier functions (dotted lines). The localization is either done with the original WB algorithm (a) or by band disentanglement with an energy window of 0–38 eV (b).

bands avoid each other and the underlying BWs carry both, π and σ type atomic orbital contributions. Using band disentanglement, we are able to follow these contributions individually. Setting out from an initial guess for π type WFs, a single smooth band can be generated starting at the third canonical band at the Γ point, passing the avoided crossing in the middle of the Brillouin zone without any kinks and wiggles and ending at the lowest band at the *X* point [see the black dots in the Fig. 2(b)]. The same holds for the two disentangled band of predominantly σ character. When going from Γ to *X*, they smoothly switch from the lower two bands to the upper two bands without being influenced by the complex structure of the canonical bands close to the multiple avoided crossing.

After having demonstrated that our projective Wannier-Boys scheme is able to separate energy bands appropriately, the effect of the disentanglement on the locality of the resulting Wannier functions should be addressed. For that purpose, we turn our attention to the more complex case of bulk materials, diamond, and silicon, in our case.

B. Diamond

Because of the rather diffuse, atom-optimized basis functions present in the original carbon cc-pVTZ basis set of Dunning,[37] (outermost *s* and *p* exponents of 0.1285 and 0.1209, respectively), it cannot be used for a Hartree-Fock calculation of bulk diamond. Hence, the outermost exponents were reoptimized by minimizing the Hartree-Fock energy per unit cell of diamond. The resulting exponents are 0.2011 for the *s* function and 0.6256, 0.3243 for the *p* functions, typical values for diamond.[39] In addition the two *d* functions of the triple-ζ basis set were replaced by the single one of the corresponding double-ζ basis set (with exponent 0.55),[37] and, as for *t*-PA, the *f* function had to be skipped because CRYSTAL cannot handle them. This basis set, referred to as bulk-optimized cc-pVTZ, has been used very successfully in our embedding studies of wave-function-based correlation calculations for diamond.[22] The experimental lattice constant of 3.57 Å (Ref. 40) is adopted which corresponds to an interatomic C–C distance of 1.546 Å, together with a $40\times40\times40$ Monkhorst-Pack grid.

Because the first four low-lying virtual bands of diamond are separated from the rest of the virtual bands by a small gap, it is possible to use the original WB algorithm to generate localized WFs ω_s. The energy bands obtained from the Wannier representation $F_{st}(\boldsymbol{R})$ of the Fock operator exactly reproduce the canonical bands [see Fig. 3(a)]. Nevertheless, the resulting localized WFs possess rather substantial tails at the second-nearest-neighbor carbon atoms as seen in Fig. 4(a). These tails can very well spoil the performance of any scheme which relies on the locality of virtual WFs (like the one used in Ref. 21).

Extending the active space used in the WB algorithm opens the possibility for making the WFs more compact. Switching to an energy window of 0–38 eV, the spread of the virtual WF, as measured by the Foster-Boys functional (3), reduces by more than a factor of 2 (see Table I) and the undesired orbital contributions at the second-nearest-neighbor carbon atoms disappear in the contour plot shown in Fig. 4(b). No shrinking of the virtual WF around the central bond is discernible in Fig. 4 compared to the WF obtained by the original WB localization. Apparently, the reduction in the spread is solely due to the fading of the tails in the localized WF, precisely what we are aiming for.

The price to pay, is an overall upward shift of the disentangled bands with respect to the canonical ones, more pro-

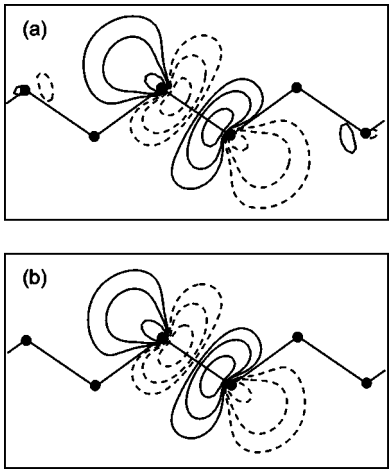

FIG. 4. Virtual WF of diamond shown in the (110) plane of a C–C zig-zag chain as obtained by the original WB algorithm (a) or by band disentanglement with an energy window of 0–38 eV (b). The values of the contours are ±0.046, ±0.10, and ±0.22 bohr$^{-3/2}$ (a geometrical progression with $q=10^{1/3}$).

nounced at the X point than at the Γ or L point, a phenomenon we also hit on for silicon in Sec. III C. It is a feature one often observes when Foster-Boys-type schemes are used to localize virtual orbitals. The localization functional Ω tries to minimize the extent of the orbitals as much as possible, regardless of the chemical nature of the orbitals and, in particular, their orbital energies. But compactness of orbitals usually implies high kinetic energies. Thus, it can easily happen that the WFs pick up more and more kinetic energy during the iterative procedure of the projective WB localization algorithm as soon as the BWs spanning the active space allow it. In practice, a compromise has to be found between tracing the proper orbital character in BWs energetically far away from the bands in mind and the risk of opening channels for spurious orbital compression.

C. Silicon

Silicon is the next and most interesting example which is discussed here, because local virtual WFs cannot be generated at all for silicon without band disentanglement.

The relativistic energy-consistent Ne-core pseudopotential from Stuttgart[41] together with a decontracted $[3s3p]$ version of the corresponding optimized valence double-ζ basis set

TABLE I. The spread Ω (per orbital) of the virtual WFs of diamond and silicon (in bohr^2) as a function of the energy window (in eV) used for the band disentanglement. For comparison, the scaled spreads Ω/a^2 with a being the lattice constant are given as well.

Diamond			Silicon		
Window	Ω	Ω/a^2	Window	Ω	Ω/a^2
None	10.10	0.792	0–15	33.03	1.120
0–38	4.94	0.388	0–31	15.45	0.524

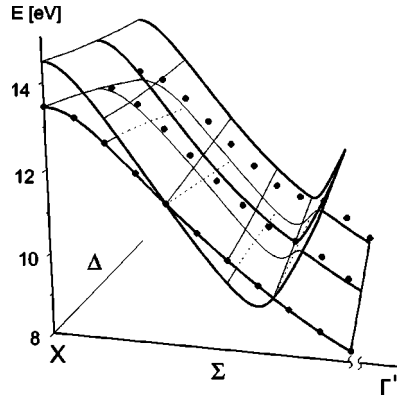

FIG. 5. Fourth and fifth conduction band of silicon in the vicinity of the two symmetry-allowed crossings on the Σ line drawn as a two-dimensional function in the $\Gamma X\Gamma'$ plane. The canonical bands are shown as energy surfaces, the uppermost disentangled band (whose energies are only available on the Monkhorst-Pack grid) as dots. An energy window of 0–15 eV is used for the disentanglement.

are used here. The basis set is augmented by a single d polarization function with an exponent of 0.4. The Si–Si distance is set to 2.352 Å which corresponds to a lattice constant of 5.432 Å. These computational parameters originate from the first pioneer study on a rigorous determination of the correlation energy of silicon by means of an incremental expansion,[5] and have successfully been used from that time on in all *ab initio* studies of correlation effects in bulk silicon performed with the incremental scheme[42,43] or its extension to valence and conduction bands.[8,9] As for diamond, a very dense $40\times40\times40$ Monkhorst-Pack grid is used here to resolve the subtle details of the silicon conduction bands to be discussed below.

The reasons why band disentanglement is absolutely crucial for silicon are the two symmetry-allowed crossings of the fourth and fifth conduction band on the Σ line from X over $U=K$ to Γ' (the $S+\Sigma$ line to be precise) which prevents a direct application of the WB algorithm (see Figs. 5 and 9). The localization simply fails because the active BWs exhibit symmetries different from the ones of the model BWs $\xi_{s\boldsymbol{k}}$ and the projection step (5) yields linear dependent projections $\xi'_{s\boldsymbol{k}}$. A d band is involved, one might speculate, but closer inspection of the corresponding BWs reveals that the fifth conduction band is an sp band, formed—in contrast to the other four conduction bands—by s and p orbitals of the next atomic shell following the $3s/3p$ valence shell, at least in the basis set employed here.

Sometimes it is argued that the band crossing problem discussed above can simply be solved by a proper relabeling of the energy bands. This is not the case. Energy bands of bulk materials are three-dimensional functions of the crystal momentum $\boldsymbol{k}$ and the two critical bands exhibit an interesting topology around the symmetry-allowed crossings. They only touch (twice), similar to the tips of two cones, as is clearly seen in Fig. 5 where the band energies are plotted as two-dimensional energy surfaces over the $\Gamma X\Gamma'$ plane. The symmetry-allowed crossings are singularities. No band crossing occurs anywhere else in the neighborhood of these

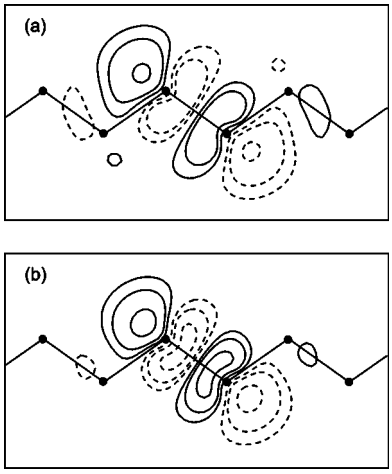

FIG. 6. Virtual WF in silicon shown in the (110) plane of a Si–Si zig-zag chain as obtained from band disentanglement with an energy window of 0–15 eV (a) or 0–31 eV (b). The value of the contours are ±0.022, ±0.046, and ±0.10 bohr$^{-3/2}$ (see Fig. 4).

points. Nevertheless, the character of the associated BWs switches from one band to the other when passing from the left- to the right-hand side of the plot plane precisely as in conventional avoided crossings no matter whether one goes along the Σ line or passes aside this high-symmetry line.

Band disentanglement is the only way out. Two different energy windows are considered, one being sort of minimal with the upper edge at 15 eV which is closely above the top of the fourth conduction band, the other being big enough to follow the BWs with proper *sp* character up to the 12th unoccupied band at $\Gamma' = 2\pi/a(1,1,1)$. In both cases, the localization could be performed without any problems. As is clearly seen in Fig. 5, the different symmetries of the fourth and fifth conduction band along the Σ line is perfectly recognized by the band disentanglement algorithm—just as for the flat *t*-PA chain discussed in Sec. III A—and the uppermost disentangled energy band exclusively follows the flatter of the two canonical bands without any kinks. Leaving the high-symmetry line, the disentangled bands start to interpolate between the two canonical bands and form a smooth and well-behaved energy surface with underlying BWs of essentially $3s/3p$ character.

The resulting localized virtual WFs of silicon are depicted in Fig. 6. Compared to diamond which exhibits typical sp^3 hybrid character around the nuclei, the virtual WF of silicon is more symmetric and *p*-like in the vicinity of the nuclei. The same holds for the maximally localized virtual WF of silicon shown in Ref. 23. Expectedly, the larger energy window yields the more compact WF and, as in the case of diamond, the reduction in the spread is impressive, from 33 down to 15 bohr^2 (Table I). Yet, all together, the virtual orbitals of silicon remain more diffuse than those of diamond even if the difference in the lattice constants is accounted for, as done by the scaled spreads listed in Table I. This is not surprising, because of the much smaller (direct) band gap of silicon (3.4 eV at Γ, experimentally)[44] compared to diamond (7.3 eV).[44]

The same conelike band touching as found for silicon also occurs for the π bands of a graphene sheet around the *K*

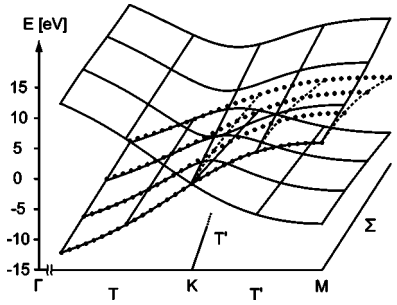

FIG. 7. The π bands (solid lines) of graphene around the *K* point together with the disentangled π band (dots) for even BWs with respect to the vertical mirror plane along the $T+T'$ line. The Fermi level is at −0.83 eV (the energy of the crossing)

points, the corners of the hexagonal first Brillouin zone (see Fig. 7). Moving along the $T+T'$ line from Γ over *K* to *M*, the character of the BWs from the lower (occupied) band changes abruptly from even to odd with respect to the vertical mirror plane along the $T+T'$ direction, when passing from inside the first Brillouin zone into the neighbor Brillouin zone. The BWs from the upper (virtual) band behave in the opposite way. Band disentanglement can be used to follow one of these characters, if one is willing to mix occupied and virtual states. This is demonstrated in Fig. 7 for the band structure calculated with an STO-3G minimal basis set for carbon, a lattice constant of 2.461 Å, and a 96×96 Monkhorst-Pack grid for the case of even BWs.

The resulting disentangled π band is smooth with a well-defined nonzero gradient $\nabla_{\boldsymbol{k}}\eta_{sk}$ at each *K* point. The band is occupied to about 85% and virtual to about 15% with the virtual contributions being restricted to the neighborhood of the T' lines parallel to the symmetry-defining vertical mirror plane. The associated WF is a well-localized bonding π orbital sitting on a C–C bond perpendicular to the mirror plane (see Fig. 8).

Let us turn back to the band structure of silicon. The complete disentangled bands are shown in Fig. 9. As already discussed above, disentangled conduction bands have the tendency to shift upward with increasing size of the energy window, a trend which is also found for silicon (see Fig. 9). Therefore, a further increase of the energy window beyond

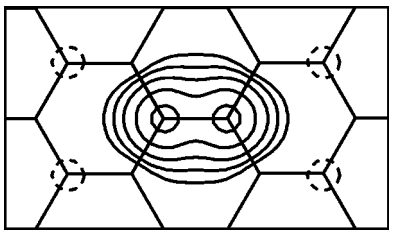

FIG. 8. Localized π type WF of graphene (plotted 0.4 Å above the molecular plane) as obtained from the disentangled band shown in Fig. 7. The values of the contours are ±0.010, 0.022, 0.046, 0.10, and 0.22 bohr$^{-3/2}$ (which are two more than in Fig. 4).

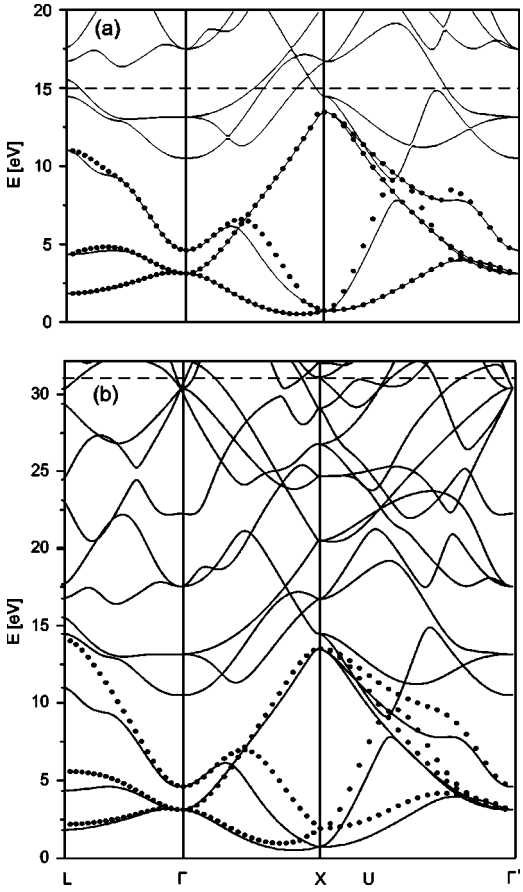

FIG. 9. Virtual Hartree-Fock band structure of silicon (solid lines) and the energies of the disentangled bands (dots) using either a 0–15 eV energy window (a) or a 0–31 eV energy window (b) for the band disentanglement.

31 eV is not very helpful anymore, although even more compact virtual WFs can be generated this way.

There exist a couple of further interesting features in the disentangled conduction bands of silicon. One is, that the second disentangled band along the Σ line climbs up to the *upper* part of the avoided crossing in the middle of the Σ panel. Apparently, close to this crossing the contaminating $4s/4p$ orbital character is solely sitting on the energetically more *stable* second BW while the corresponding valence $3s/3p$ contributions form the fourth BW, an interpretation which is corroborated by a detailed analysis of the involved BWs.

The second point is the unexpected discontinuity in the uppermost disentangled band along the Σ line discernible in Fig. 9(a) for the 0–15 eV window. Its position coincides with the position of the avoided crossing between the sixth and eighth conduction band which shows up in the middle of the Σ panel between 15 and 18 eV. During the band disentanglement, the BWs from the upper part of this crossing are excluded from the active space while those of the lower part are present, and it seems that there is still a substantial part of the necessary orbital character present in this upper BWs to cause the abrupt change in the uppermost disentangled band. Obviously, the $3s/3p$ valence orbital character moves up much higher into the unoccupied band structure of silicon than one might expect at first glance.

This is the reason why we switched to the larger energy window of 0–31 eV, though a non-negligible upward shift of the disentangled virtual bands arises. Nevertheless, we consider the disentangled bands and Bloch orbitals from the enlarged energy window to be the more appropriate ones.

IV. CONCLUSIONS

An extension of the Wannier-Boys localization algorithm for periodic systems[18,19] is developed which allows to generate localized WFs in the case of *entangled* energy bands. The method has been implemented into the localization routine of the CRYSTAL program package.[35] Its main feature is the use of an enlarged set of active BWs during the optimization of the unitary hybridization matrix for the multiband Wannier transformation. This allows the inclusion of *all* BWs which contain noticeable admixture from orbitals with the same chemical character as the localized Wannier functions one is looking for. The proper identification of these admixtures is done by a simple projection technique.

The efficiency of our projective Wannier-Boys algorithm is demonstrated for the virtual bands of three different systems, *t*-PA, diamond, and bulk silicon. Localized *virtual* Wannier functions could be generated in all three cases. The spatial extent of them is found to be controllable by the size of the active space, i.e., the number of selected Bloch waves per k point. The more Bloch waves are considered, the more compact the localized Wannier functions become. Yet, at the same time, an increasing tendency for an overall upward shift in the energies of the disentangled bands is observed.

The same trend is discernible in the Kohn-Sham energies of silicon discussed by Souza *et al.*,[23] though, because of the tight energy window employed there (up to $\sim$11 eV), the effect is not very pronounced. The spread of the maximally localized virtual Wannier function of silicon reported there is 30.13 bohr^2 (based on a $10\times10\times10$ Monkhorst-Pack grid) which is quite close to the value of 33.03 bohr^2 we found for the 0–15 eV energy window.

Even metallic bands can be disentangled by the projective Wannier-Boys algorithm as is demonstrative exemplarily for the π bands of a graphene monolayer.

The choice of the systems considered here was not accidental. Subsequent use of the localized Wannier functions in wave-function-based post-Hartree-Fock correlation methods for periodic systems which explicitly exploit the local character of virtual WFs was the driving force of this work, for example the method used in our study of the valence and conduction bands of *t*-PA (Ref. 21) or in analogue investigations of the band structure of bulk materials like diamond.[22] The more compact the WFs are the better these local correlation methods perform.

ACKNOWLEDGMENTS

We thank the CRYSTAL group in Torino for making available to us the source code of the CRYSTAL 200x code without which the present study would not have been possible.

*Corresponding author. Electronic address: birken@mpipks-dresden.mpg.de
†Electronic address: izotov@mpipks-dresden.mpg.de

[1] G. Wannier, Phys. Rev. **52**, 191 (1937).
[2] R. D. King-Smith and D. Vanderbilt, Phys. Rev. B **47**, R1651 (1993).
[3] R. Resta, Europhys. Lett. **22**, 133 (1993).
[4] R. Resta, Rev. Mod. Phys. **66**, 899 (1994).
[5] H. Stoll, Chem. Phys. Lett. **191**, 548 (1992).
[6] H. Stoll, Phys. Rev. B **46**, 6700 (1992).
[7] J. Gräfenstein, H. Stoll, and P. Fulde, Chem. Phys. Lett. **215**, 611 (1993).
[8] J. Gräfenstein, H. Stoll, and P. Fulde, Phys. Rev. B **55**, 13 588 (1997).
[9] M. Albrecht, P. Fulde, and H. Stoll, Chem. Phys. Lett. **319**, 355 (2000).
[10] E. I. Blount, *Solid State Physics* (Academic Press, New York, 1962), Vol. 13, p. 305.
[11] C. Edmiston and K. Ruedenberg, Rev. Mod. Phys. **35**, 457 (1963).
[12] W. Kohn, Phys. Rev. B **7**, 4388 (1973).
[13] V. P. Smirnov and D. E. Usvyat, Phys. Rev. B **64**, 245108 (2001).
[14] S. F. Boys, Rev. Mod. Phys. **32**, 296 (1960).
[15] J. M. Foster and S. F. Boys, Rev. Mod. Phys. **32**, 300 (1960).
[16] N. Marzari and D. Vanderbilt, Phys. Rev. B **56**, 12 847 (1997).
[17] G. Berghold, C. J. Mundy, A. H. Romero, J. Hutter, and M. Parrinello, Phys. Rev. B **61**, 10 040 (2000).
[18] P. Baranek, C. M. Zicovich-Wilson, C. Roetti, R. Orlando, and R. Dovesi, Phys. Rev. B **64**, 125102 (2001).
[19] C. M. Zicovich-Wilson, R. Dovesi, and V. R. Saunders, J. Chem. Phys. **115**, 9708 (2001).
[20] R. Resta, Phys. Rev. Lett. **80**, 1800 (1998).
[21] V. Bezugly and U. Birkenheuer, Chem. Phys. Lett. **399**, 57 (2004).
[22] C. Willnauer, M. von Arnim, W. Alsheimer, D. Izotov, U. Birkenheuer, V. R. Saunders, R. Dovesi, and C. M. Zicovich-Wilson (unpublished).
[23] I. Souza, N. Marzari, and D. Vanderbilt, Phys. Rev. B **65**, 035109 (2001).
[24] V. R. Saunders, R. Dovesi, C. Roetti, R. Orlando, C. M. Zicovich-Wilson, N. M. Harrison, K. Doll, B. Civalleri, I. J. Bush, P. D'Arco, and M. Llunell, *CRYSTAL2003 User's Manual* (Universitá di Torino, Torino, 2003).
[25] J. A. Pople *et al.*, *Gaussian 03* (Gaussian, Inc., Pittsburgh PA, 2003).
[26] B. Delley, J. Chem. Phys. **113**, 7756 (2000). (DMol^3 is available as part of the Materials Studio by Accelrys, Inc.).
[27] M. Methfessel, M. van Schilfgaarde, and R. A. Casali, in *Electronic Structure and Physical Properties of Solids: The Uses of the LMTO Method*, edited by H. Dreysse, Lecture Notes in Physics Vol. 535, (Springer, Berlin 2000).
[28] G. te Velde, E. J. Baerends, P. H. T. Philipsen, G. Wiesenekker, J. A. Groeneveld, F. Kootstra, P. L. de Boeij, and J. G. Snijders, *BAND2004* (SCM, Theoretical Chemistry, Vrije Universiteit, Amsterdam, 2004).
[29] E. J. Baerends *et al.*, *ADF2004* (SCM, Theoretical Chemistry, Vrije Universiteit, Amsterdam, 2004).
[30] C. M. Zicovich-Wilson and R. Dovesi (private communication).
[31] R. S. Mulliken, J. Chem. Phys. **23**, 1833 (1955).
[32] R. S. Mulliken, J. Chem. Phys. **23**, 1841 (1955).
[33] P.-O. Löwdin, J. Chem. Phys. **18**, 367 (1950).
[34] E. Hückel, Z. Phys. **70**, 204 (1931).
[35] V. R. Saunders, R. Dovesi, C. Roetti, M. Causà, N. M. Harrison, R. Orlando, C. M. Zicovich-Wilson, K. Doll, and B. Civalleri, *CRYSTAL200x User's Manual* (Universitá di Torino, Torino, 2001).
[36] H. J. Monkhorst and J. D. Pack, Phys. Rev. B **13**, 5188 (1976).
[37] T. H. Dunning, J. Chem. Phys. **90**, 1007 (1989).
[38] U. Birkenheuer, J. Chem. Phys. **110**, 7449 (1999).
[39] R. Orlando, R. Dovesi, C. Roetti, and V. R. Saunders, J. Phys.: Condens. Matter **2**, 7769 (1990).
[40] N. W. Ashcroft and S. D. Mermin, *Solid State Physics* (Saunders, Philadelphia, 1976), Table 4.3.
[41] A. Bergner, M. Dolg, W. Kuchle, H. Stoll, and H. Preuss, Mol. Phys. **80**, 1431 (1993).
[42] B. Paulus, P. Fulde, and H. Stoll, Phys. Rev. B **51**, 10 572 (1995).
[43] B. Paulus, K. Rościszewski, H. Stoll, and U. Birkenheuer, Phys. Chem. Chem. Phys. **5**, 5523 (2003).
[44] R. W. Godby, M. Schlüter, and L. J. Sham, Phys. Rev. B **36**, 6497 (1987).